



Validating dilute settling suspensions numerical data through MRI, UVP and EIT measurements

R. Silva^{a,*}, F.A.P. Garcia^a, P.M. Faia^b, Paul Krochak^c, Daniel Söderberg^d, Fredrik Lundell^d, M.G. Rasteiro^a

^a Chemical Engineering Department, Faculty of Sciences and Technology of the University of Coimbra, and CIEPQPF – Research Centre on Chemical Process and Forest Products, Polo 2, Pinhal de Marrocos, 3030-790 Coimbra, Portugal

^b Electrical and Computers Engineering Department, Faculty of Sciences and Technology of the University of Coimbra and CEMUC – Centre of Mechanical Engineering, Polo 2, Pinhal de Marrocos, 3030-290 Coimbra, Portugal

^c Innventia AB, SE-114 86, Stockholm, Sweden

^d Wallenberg Wood Science Centre, Royal Institute of Technology, KTH Mechanics, SE 100 44 Stockholm, Sweden

ARTICLE INFO

Article history:

Received 23 August 2015

Received in revised form

22 April 2016

Accepted 4 June 2016

Available online 6 June 2016

Keywords:

Mixture model

Solid–liquid suspensions

Magnetic resonance imaging

Electrical impedance tomography

Ultrasonic velocity profiling

ABSTRACT

The measurement of fluid dynamic quantities are of great interest both for extending the range of validity of current correlations to be used in equipment design and for verification of fundamental hydrodynamic models. Studies where comparisons are made between imaging techniques serve to provide confidence on the validity of each technique for the study of multiphase flow systems. The advantage of cross-validation is that it can help establish the limitations of each technique and the necessary steps towards improvement. A small amount of comparative studies are found in the literature and none of them reports the study of settling particles suspension flow using simultaneously Ultrasonic Velocity Profiling (UVP), Magnetic Resonance Imaging (MRI) and Electrical Impedance Tomography (EIT), at least not to the best of the authors knowledge. In the present paper the authors report efforts made on the characterization of dilute suspensions of glass particles in turbulent flow, with increasing flow velocities and particles concentrations, in a pilot rig at a laboratorial scale, using both MRI, EIT and UVP: direct comparisons of EIT, MRI and UVP measurements acquired and mixture model numerical simulations are presented and the level of agreement explored.

© 2016 Elsevier Ltd. All rights reserved.

1. Introduction

The application of settling suspensions in industrial environments has become widespread; however, as a result of their innate complexity there is no unified predictive numerical model or empirical correlation to predict the flow characteristics (pressure drop, flow regime, etc.) [1,2]. When working with settling suspensions a number of variables have to be accounted as flow patterns, transition velocities, the flow behaviour in pipes of different geometries, and also particle concentration, particle shape, size, and size distribution. Industries still rely on custom charts or data for their particular suspension flow, which is rather inefficient resulting in oversized dimensioning, low energy efficiency and even operation limitations/difficulties. The design and scale-up of equipment for multiphase flows are still predominantly based on empirical correlations validated over a limited range of operating conditions and physical properties. Application of more fundamental fluid dynamic

numerical models awaits their experimental verification. Hence, measurement of fluid dynamic quantities such as phase velocities, phase holdups, bubble size etc. are of great interest both for extending the range of validity of current correlations and for verification of fundamental hydrodynamic models.

Tomography offers a unique opportunity to reveal the complexities of the internal structure of an object without the need to invade it. Magnetic Resonance Imaging (MRI) is a high spatial resolution tomographic technique with the ability to provide information about the behaviour of protons present in a system, usually contained in the 1H nuclei of water. Amongst others, MRI is used to image motion of water expressed in the form of velocity profiles. The major limitations of MRI are the types of particles and the size of the system that can be studied, together with the size, weight and cost of the instrument. Only particles containing MR-sensitive nuclei, such as 1H, can be detected [3,4]. The maximum diameter of the system is bounded by the inner diameter of the coil in the magnet. Thus, MRI experiments are typically limited to laboratory-scale fluidised beds or small diameter pipes [5]. In summary, the strength of MRI is in studying centimetre-scale systems at spatial resolutions of approximately 100 μm . Electrical

* Corresponding author.

E-mail address: rsilva@eq.uc.pt (R. Silva).

Nomenclature

EIT	Electrical Impedance Tomography	ϕ_{max}	Maximum packing of solids
ID	Internal diameter	A_{σ}	Area under the normalized electrical conductivity curve
MRI	Magnetic Resonance Imaging	c_d	Dispersed phase mass fraction
UPV	Ultrasound Pulse Velocimetry	C_D	Drag coefficient
UVP	Ultrasound Doppler Velocimetry Profiling	$C_{\varepsilon 1}$	Closure coefficient for the k - ε turbulence model
∇	Mathematical gradient	$C_{\varepsilon 2}$	Closure coefficient for the k - ε turbulence model
$\nabla \cdot$	Mathematical divergence	σ_{ε}	Closure coefficient for the k - ε turbulence model
δ	First gradient pulse duration	σ_k	Closure coefficient for the k - ε turbulence model
ΔP	Pressure drop	C_{μ}	Closure coefficient for the k - ε turbulence model
ε	Turbulent dissipation rate	d_p	Particle diameter
η	Normalized conductivity	D_{md}	Turbulent eddy diffusion
μ_m	Mixture dynamic viscosity	D_t	Scalar diffusivity coefficient
μ_c	Dynamic viscosity of the continuous phase	F	Volume forces
μ_d	Dynamic viscosity of the dispersed phase	g	Gravitational acceleration
ν	Mixture kinematic viscosity	I_T	Turbulence intensity
ν_T	Turbulent kinematic viscosity	k	Turbulent kinetic energy
ρ_m	Mixture density	L	Characteristic length of the equipment
$\rho_c; \rho_L$	Continuous phase density	L_T	Turbulence length scale
$\rho_d; \rho_s$	Dispersed phase density	m_{dc}	Mass transfer ratio between phases
τ_{Gm}	Turbulent and viscous stresses	p_m	Pressure of the mixture
σ	Electrical conductivity	P_k	Turbulence production
σ_m	Mixture electrical conductivity	Re_p	Particle Reynolds Number
σ_0	Reference electrical conductivity	T_i	Turbulence intensity
σ_w	Water electrical conductivity	u_m	mixture velocity
σ_{s0}	Electrical conductivity for a known initial concentration of solids	u_{mk}	Velocity of phase k in function of the center of the mass of the mixture.
σ_T	Particle Schmidt Number	u^T	Transpose of the mixture velocity
ϕ_{ap}	Apparent solids concentration	u_c	Continuous phase velocity
ϕ_c	Continuous phase volumetric fraction	u_d	Dispersed phase velocity
$\phi; \phi_d$	Dispersed phase volumetric fraction	$U V W$	Velocity in the x, y and z directions, respectively.
ϕ_k	Volumetric concentration of phase k	V_k	Volume of particle
ϕ_0	Initial concentration of solids	y^+	Wall lift-off in viscous units
$\phi(z)$	Calculated vertical particle distribution profile	y_p	Distance from the wall

Impedance Tomography (EIT) can be used to study much larger-scale systems and gives good quality qualitative images of gas–liquid–solid distributions [6]. The main advantages of EIT are its portability, simplicity of scale up, and relative low cost. Spatial resolution, however, is typically limited: this is due to both the reconstruction algorithms used (the nature of the reconstruction problem posed by EIT, which is ill conditioned and non-linear, makes the detection of small objects a challenge) and the number of unique measurements of conductivity obtainable, as derived from the current injection-voltage measurement system (very strongly dependent on the number of measuring electrodes) [7]. Furthermore, information concerning the absolute amount of solids suspended, cannot be accurately determined, since the images obtained represent not absolute values of the conductance/impedance, but the distribution of their variation. The measurement of instantaneous velocities in water flows has long been a challenging issue. Due to their relatively low price and easy handling, Acoustic Doppler systems are widely used at present. Ultrasound systems, based on echography and Doppler Effect, allowed the development of equipment capable of measuring almost instantaneous velocity profiles [8,9]. Initially, the Ultrasonic Velocity Profiling (UVP) technique was limited to opaque fluids [10] and it was typically used to measure across pipe walls at small scale pressure [11]. An UVP probe emits an ultrasound beam that travels along the incident axis and, afterwards, receives the echo from the same beam after reflection by small particles present in the fluid. The UVP system measures the time delay of the echo to reach the

probe and the Doppler frequency shift. Knowing the speed of the sound in the fluid, the distance to and the velocity of the particle in the direction of the beam can be calculated. Although the UVP technique has been developed for 1D measurements, measurement of 2D velocity fields using UVP probes have been reported to give promising results [8,9].

Detailed reviews on experimental tomographic techniques are given in the literature [12–14] where comparisons are made between imaging techniques which serve to provide confidence on the validity of each technique for the study of multiphase flow systems. The advantage of cross-validation is that it can help establish each the limitations of each technique and the necessary steps towards improvement. Magnetic resonance imaging, ultrasonic pulsed Doppler velocimetry, electrical impedance tomography, x-ray radiography and neutron radiography are shown to be capable of measuring the distribution of solids in suspensions [12], while only the velocity profiles are attained with magnetic resonance imaging and ultrasonic pulsed Doppler velocimetry. These reviews serve as a guide to identify suitable methods to meet specific measurement requirements through a broad analysis of the basic theory of each individual technique as well as their merits in acquiring velocity, size, shape and concentration measurements of particulate mixtures [13]. Additionally, they serve as a summary on the progress and developments in velocimetry techniques and flow imaging techniques [14]. However, the cross-validation between these techniques in each of the reviews is limited to two techniques at a time, either comparing velocity or

concentration profiles for the same case study. So, a small amount of comparative studies are found in the literature and none of them reports the study of settling particles suspension flow using simultaneously UVP, MRI and EIT, at least not to the best of the authors knowledge. In the following section, first, the experimental and numerical methods and models are introduced. The results are presented and discussed in the following order: (i) MRI, UVP and simulated velocity data from a pipe with 0.34 m inner diameter (ii) EIT particle concentration data from a pipe with 0.50 m inner diameter and (iii) MRI, UVP and simulated velocity data from a pipe with 0.50 m inner diameter. The conclusions are summarised after the presentation and discussion of the data.

2. Experimental setup and conditions

In this section the experimental conditions employed in the study of dilute solid-liquid suspensions flow are described. The tests were performed in the joint recirculatory pipe flow facility of KTH Royal Institute of Technology and Innventia AB in Stockholm, Sweden. Two different configurations were assembled to perform tests with two different internal pipe diameters, 0.34 and 0.50 m. The test sections of the flow loop for both configurations were built from cylindrical Perspex® piping possessing a total length of 7.0 m which allowed the flow to be fully developed at the measuring sections. The schematics of the flow loop can be observed in Fig. 1.

The solid-liquid suspensions were composed of Type S Silibeads® spherical glass beads, provided by Sigmund Lindner GmbH, and tap water. The tests were performed some time (approximately 10 min) after the pump had been started in order to ensure that the flow had stabilized. The spherical glass beads size, concentrations and flow rates employed are summarized in Table 1.

3. Experimental tomographic techniques

In this study MRI, UVP and EIT tomographic techniques were employed in the study of dilute solid-liquid suspensions flow. The vertical and horizontal velocity profiles for both liquid and solids using the MRI and UVP, respectively, were attained with these experimental techniques. Moreover, the EIT apparatus was used to obtain data regarding the distribution of particles in the pipe section.

Table 1

Solid-liquid suspensions experimental conditions for the performed tests.

				$Q [l. s^{-1}]$	$U [m. s^{-1}]$	Re
0.34 m ID Pipe						
$d_{p50} [mm]$	0.15	$\phi [v/v]$	0.005	1.0	1.10	36641
				2.0	2.20	73281
				0.01	1.0	1.10
	0.03	1.0	1.10	2.0	2.20	73281
				1.0	1.10	36641
				2.0	2.20	73281
$d_{p50} [mm]$	0.15	$\phi [v/v]$	0.005	1.0	1.10	36641
				2.0	2.20	73281
				0.01	1.0	1.10
	0.03	1.0	1.10	2.0	2.20	73281
				1.0	1.10	36641
				2.0	2.20	73281
0.50 m ID Pipe						
$d_{p50} [mm]$	0.5	$\phi [v/v]$	0.01	2.0	1.02	49831
				4.0	2.04	99662
				0.03	2.0	1.02
	0.05	2.0	1.02	4.0	2.04	99662
				2.0	1.02	49831
				4.0	2.04	99662

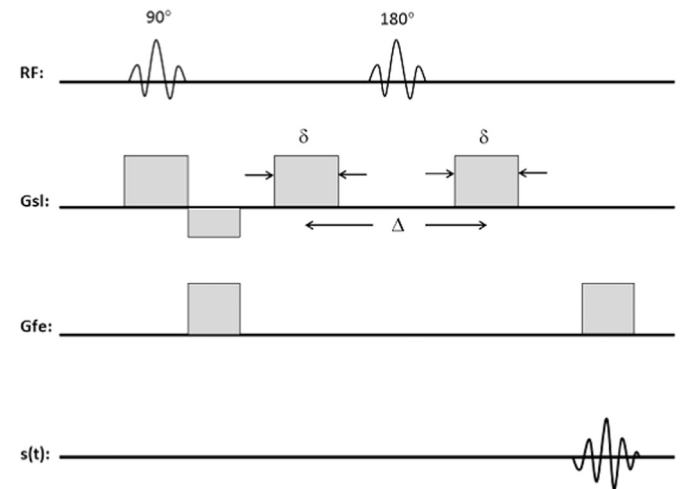


Fig. 2. Radiofrequency and magnetic pulse sequence used to obtain NMR velocity profile images for the flow of water in the pipe. G_{sl} is the slice selection gradient and G_{fe} is the frequency selection gradient. The slice selection gradient is used for flow encoding.

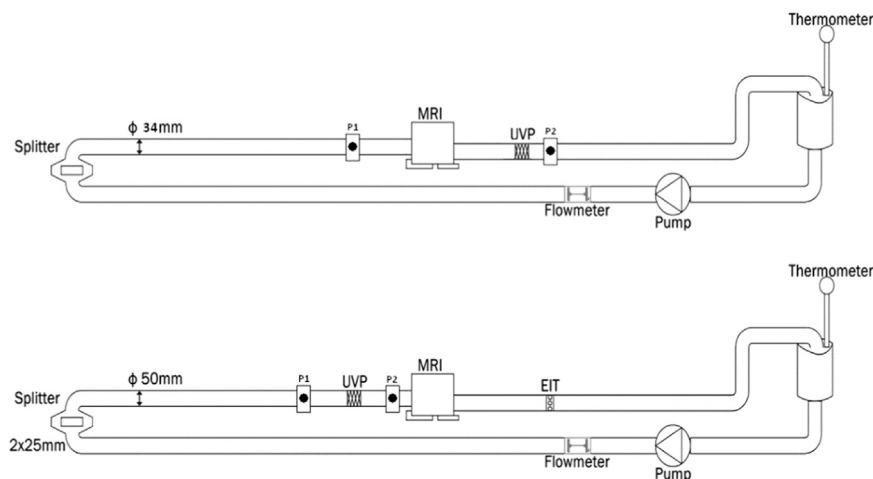


Fig. 1. Schematics of the flow loops with 34 (Top) and 50 (Bottom) mm ID pipes.

3.1. Magnetic Resonance Imaging (MRI)

With this study, for the MRI flow characterization, a gradient-echo pulse sequence was used (see Fig. 2). A detailed description of this technique is found in the literature [15]. The technique can be summarized as selective excitation of a streamwise slice of fluid and a 90° radiofrequency (RF) pulse rotating the magnetization orthogonally. A first phase-encoding gradient pulse is then applied for a duration, δ , giving each spin a spatially dependent phase offset. A 180° RF pulse is then applied rotating each spin isochromat (a microscopic group of spins, which resonate at the same frequency) through 180°. A second phase-encoding gradient pulse is applied at a time Δ after the first one to obtain a phase offset relative to the fluid displacement. A frequency position encode gradient is applied during readout.

Throughout the experiments, the phase dispersion is sensitive to the mean and fluctuating velocities; therefore, the duration and separation times for the phase flow encoding gradients need to be adjusted manually. For the higher speed flow, i.e., for $U=2.2 \text{ m}\cdot\text{s}^{-1}$ (see Table 1) profiles were averaged over 128 individual measurements and 64 measurements were averaged for lower flow rates. In all cases the slice was 10 mm long and the gain was on the order of 1000 dB. The MRI system consists of a 1 T permanent magnet connected to a Bruker NMR spectrometer. A 60 mm RF coil, calibrated to 43.5 MHz is used for transmission/reception. The entire system has been provided by Aspect Imaging® and is controlled using NTNMR® software. Devoted measurement and data processing software was developed at the University of California Davis and further adapted in-house for post-processing [16].

3.2. Ultrasonic Velocity Profiling (UVP)

Ultrasonic Velocity Profiling (UVP), also designated Ultrasound Doppler Velocimetry Profiling (UVP), was utilized to measure the velocity of the particles. UVP fundamentals have been well documented in the literature [8,9]. In the studies presented in this manuscript a 4 MHz transducer with a 5 mm active diameter element (maximum resolution of 0.37 mm) and a minimum measuring distance (near field) of 16.9 mm was used. After this minimum, the beam diverges with a half-angle of 2.2°. The pulse repetition frequency was 10.762 kHz with 128 spatial measurement channels. Data was acquired over 768 measurement cycles to obtain a velocity distribution profile and mean data was obtained by averaging over 64 profiles, providing a spatial and velocity resolutions of 0.37 mm and 3.8 mm/s, respectively. The transducers were flush mounted to the inside pipe wall at a 70 degree angle to the flow and were in direct contact with the suspension (see Fig. 3).

With this approach, the effects of attenuation and wall reflections were reduced. The UVP hardware was provided by Met-Flow® and the software, FlowViz®, was developed by SIK - The Swedish Institute for Food and Biotechnology in Gothenburg,

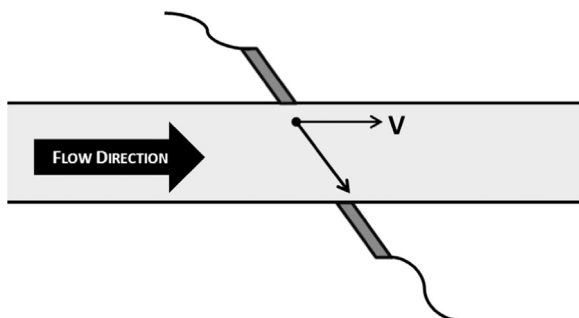


Fig. 3. General set-up for the UVP probe system.

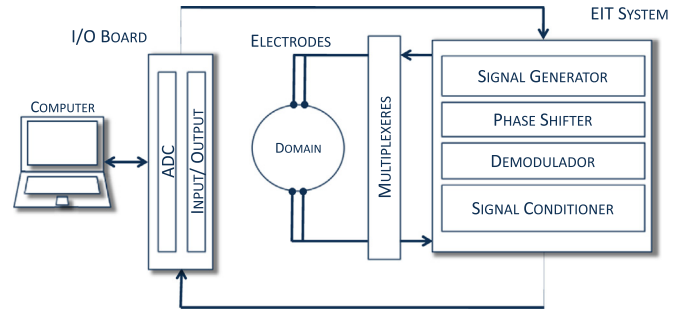


Fig. 4. Block diagram of the EIT system employed in this study.

Sweden [17,18].

3.3. Electrical Impedance Tomography (EIT)

The EIT system used in the studies depicted in this manuscript) has already been described in the literature [19,20]. The system is composed of function specific modules: signal generation and phase shifting occur on the same module, signal multiplication, demodulation and conditioning are done in another module and multiplexing is done in a third module. In EIT an electrical current is injected through a set of pair of electrodes placed in the boundary of the domain under study (see Fig. 4), thereby resulting an electrical field that is conditioned by the materials distribution within the domain.

The resulting electrical potentials in the domain perimeter can be measured using the remaining electrodes, and those values are fed to a non-linear inverse algorithm to attain the previously unknown conductivity/resistivity distribution. The procedure is only complete when all electrodes are used for injection or projection, so the cycle has as many projections as the number of electrodes (see Fig. 5).

For the depicted tests an EIT test section with 16 titanium electrodes was produced: each electrode has a diameter of 5 mm, which were previously optimized and equally spaced around the test section perimeter. In all the tests an excitation frequency of 10 kHz with 2 V peak-to-peak amplitude was used: adjacent injection and measuring protocols were used. For image reconstruction, the open source software EIDORS [21], considering direct differential measured voltages and using a structured Mesh consisting of 2304 linear elements and 1201 nodes was used (in the reconstructed images the electrode corresponding to higher vertical position is electrode number 1). This software implements a non-linear back projection method using a regularization algorithm (Tikhonov's regularization) [22]. To solve the forward problem the Complete Electrode model (CEM) [23] was chosen: this model incorporates the shunt effect and the contact impedance in the electrode/domain interface.

In the present study an in house built EIT apparatus was employed to obtain vertical concentration profiles through normalized electrical conductivity measurements. The normalization is done using the reference measurements for tap water without particles, as described by Eq. (1)

$$\eta = \frac{\sigma_0 - \sigma_m}{\sigma_0} \quad (1)$$

To accomplish the proposed endeavour two approaches were used to attain the vertical particle distributions: the first approach was based on the Maxwell Equation, which is one of the most widely used equations that correlates the electrical conductivity with particle concentration, and has shown great promise in deposition recognition [24] and depicting the asymmetry in swirling flows [25]. Since all particles involved in this study are non-

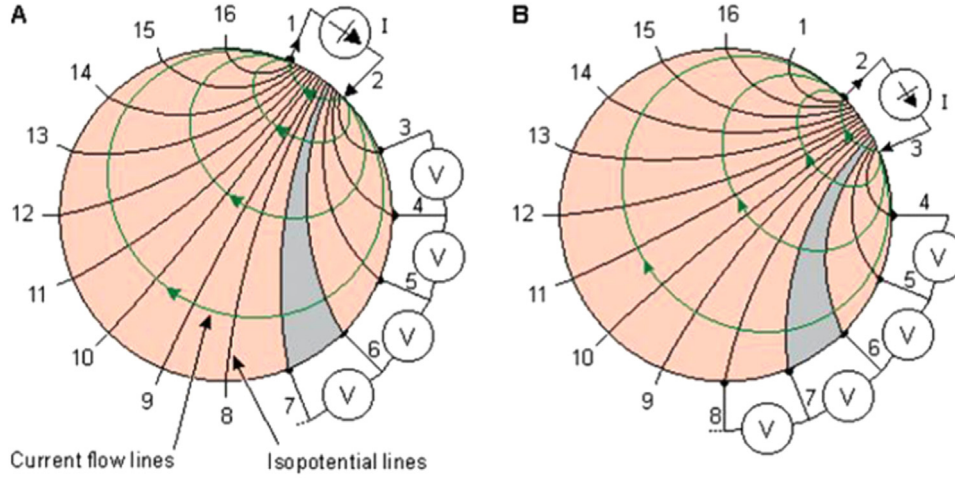


Fig. 5. EIT injection and measurement protocols for the first (A) and second (B) projections. Adapted from [23].

conducting settling particles, one of the approaches to achieve vertical particle distributions will be to directly use the Maxwell Equation (see Eq. 2)

$$\sigma_m = \sigma_w \left(\frac{2 - 2\phi_0}{2 + \phi_0} \right). \quad (2)$$

Using the studies by Giguère et al. [26] as the basis, where the normalized electrical conductivity, η , is combined with Eq. (2), and through algebraic manipulation, Eq. (3) is obtained for the apparent solids concentration, ϕ_{ap} :

$$\phi_{ap} = \frac{2 - 2((1 + \eta)(\sigma_0/\sigma_{s0}))}{2 - ((1 + \eta)(\sigma_0/\sigma_{s0}))}, \quad (3)$$

where the σ_0/σ_{s0} quantity is achieved using the known initial concentration of solids, ϕ_0 , as the initial condition in Eq. (2). This assumes a homogenous particle distribution which is contrary to the observed experimental flow regimes.

In order to avoid the homogeneous particle distribution and provide a more accurate description of the particle distribution, based on the normalized electrical conductivity profiles, the following assumption was made where the initial concentration of solids is multiplied by the normalized electrical conductivity:

$$\sigma_m = \sigma_w \left(\frac{2 - 2\eta\phi_0}{2 + \eta\phi_0} \right). \quad (4)$$

With Eq. (4) the new σ_0/σ_{s0} quantity is calculated and then used in Eq. (3) to calculate the apparent solids concentration.

The second approach was to calculate the area under the normalized electrical conductivity curve, A_σ , and obtain the vertical particle distribution according to Eq. (5),

$$\phi(z) = \frac{\phi_0}{A_\sigma} \eta. \quad (5)$$

4. Numerical studies

The numerical results presented in this manuscript were attained using the mixture model in the COMSOL Multiphysics[®] software. These numerical simulations were conducted by emulating the flow conditions depicted in Table 1 until mesh independent results were attained. The mixture model is a single fluid Euler–Euler model [27–30] in which the phases consist of a

dispersed phase (solid particles, liquid droplets, etc.) and a continuous phase (liquid). It is translated by a momentum equation (Eq. (6)) and a continuity equation for the mixture (Eq. (7)). An additional term is included to describe the effect of the velocity difference between the phases (Eq. (8)). Its application is conditioned by the following assumptions: each phase density is constant, both phases share the same pressure field, and the velocity difference between phases is determined assuming that pressure, gravity and viscous drag are all balanced.

$$\rho u_t + \rho(u \cdot \nabla)u = -\nabla p - \nabla \cdot (\rho c_d(1 - c_d)u_{SLIP}u_{SLIP}) + \nabla \cdot \tau_{Gm} + \rho g + F \quad (6)$$

$$\rho_c - \rho_d \left[\nabla \cdot (\phi_d(1 - c_d)u_{SLIP} - D_{md}\nabla\phi_d) + \frac{m_{dc}}{\rho_d} \right] + \rho_c(\nabla \cdot u) = 0 \quad (7)$$

$$u_d - u_c = u_{cd} = u_{SLIP} - \frac{D_{md}}{(1 - c_d)} \nabla\phi_d \quad (8)$$

The use of a turbulence model is justified by the values of the Reynolds Number (Re) in Table 1. Additionally to a turbulence closure, a model for the interphase forces, namely the drag force, is needed. Since the choice of a drag model is dependent on Particle Reynolds Number (Re_p) range it is necessary to have a good estimate of this value. Adding on the particle data in Table 1, the calculated Particle Stokes Number (St_p) and Particle Reynolds Number as well as the Terminal Velocity c can be seen below in Table 2. Since $Re_p > 1$ and the solid-liquid suspensions are dilute, in all experimental cases, the Schiller–Naumann correlation [31] was chosen for the drag force modelling. The highest St_p is 2.20 for the bigger particles in the 0.34 m ID pipe, while the remaining values are all close to one, thus validating the application of the mixture model in these studies [27,32,33].

4.1. Drag correlations

The velocity between phases, u_{slip} , was obtained using the Schiller–Naumann [34] correlation for the calculation of the drag coefficient, C_D :

$$C_D = \begin{cases} \frac{24}{Re_p} (1 + 0.15 Re_p^{0.687}) & Re_p < 1000 \\ 0.44 & Re_p > 1000 \end{cases} \quad (9)$$

$$Re_p = \frac{d_p \rho_c |u_{SLIP}|}{\mu} \quad (10)$$

4.2. Turbulence closure

The High Reynolds k – ϵ turbulence model, in general, adds two

Table 2
Particle data for the simulations of the solid-liquid suspensions flows.

Particle Data	0.34 m ID Pipe		0.50 m ID Pipe
d_{p50} [mm]	0.15	0.5	0.5
ρ_p [kg. m ⁻³]	2500	2500	2500
U [m.s ⁻¹]	0.55 1.10 2.20	0.55 1.10 2.20	0.51 1.02 2.04
ϕ [v/v]	0.005 0.01 0.03	0.005 0.01 0.03	0.01 0.03 0.05
St_p	0.05 0.10 0.20	0.55 1.10 2.20	0.42 0.83 1.66
V_T [m.s ⁻¹]	0.018	0.200	0.200
Re_p	2.65	98.2	98.2

extra transport equations that are solved for two additional variables: the turbulent kinetic energy, k , and the dissipation rate of the turbulent kinetic energy, ε . The following equations define the High Reynolds k - ε Turbulence Model, which is incorporated in the mixture model [35].

The Turbulent Eddy Viscosity is defined as:

$$\mu_T = \rho C_\mu \frac{k^2}{\varepsilon}, \quad (11)$$

the turbulent kinetic energy, k , being given by:

$$\rho \frac{\partial k}{\partial t} + \rho u \cdot \nabla k = \nabla \cdot \left(\left(\mu + \frac{\mu_T}{\sigma_k} \right) \nabla k \right) + P_k - \rho \varepsilon, \quad (12)$$

where:

$$P_k = \mu_T \left(\nabla u : (\nabla u + (\nabla u)^T) - \frac{2}{3} (\nabla \cdot u)^2 \right) - \frac{2}{3} \rho k \nabla \cdot u, \quad (13)$$

and finally the dissipation rate, ε , is obtained through:

$$\rho \frac{\partial \varepsilon}{\partial t} + \rho u \cdot \nabla \varepsilon = \nabla \cdot \left(\left(\mu + \frac{\mu_T}{\sigma_\varepsilon} \right) \nabla \varepsilon \right) + C_{\varepsilon 1} \frac{\varepsilon}{k} P_k - C_{\varepsilon 2} \rho \frac{\varepsilon^2}{k}, \quad (14)$$

where the closure coefficients ($C_{\varepsilon 1} = 1.44$; $C_{\varepsilon 2} = 1.92$; $C_\mu = 0.09$; $\sigma_k = 1.0$; $\sigma_\varepsilon = 1.3$) were obtained empirically [35].

The turbulence modelling must also take into account the dispersed phase velocity. This is accomplished calculating the diffusion coefficient for the particle (Eq. (16)), which is a function of the turbulent particle Schmidt number [27]. The turbulent Schmidt number (σ_T) is defined as the ratio between the turbulent kinematic viscosity and the scalar diffusivity coefficient [36], and it is related to the diffusion of the particles. A default value of 0.35 is present in most commercial codes and most authors accept this value [37]. Thus, σ_T and D_{md} are:

$$\sigma_T = \frac{\nu}{D_t} \quad (15)$$

$$D_{md} = \frac{\mu_T}{\rho \sigma_T} \quad (16)$$

4.3. Boundary conditions

Additionally, the following boundary conditions were enforced on the numerical studies:

4.3.1. Inlet

At the inlet the initial velocities were imposed in the direction perpendicular to the pipe section and the turbulence intensity and length scales are as depicted below. When conceiving a CFD simulation a user seldom has knowledge on the distributions for k and ε at the inlet. To circumvent this lack of information k and ε inlet values for internal flows can be estimated, taking the turbulence intensity scale and the turbulent length scale as a starting point, using the following expressions [38]:

$$k = \frac{3}{2} (u_{I_T})^2 \quad (17)$$

$$\varepsilon = \frac{3}{2} C_\mu^{3/4} \frac{k^{3/2}}{L_T} \quad (18)$$

4.3.2. Outlet and symmetry axis

Additionally, at the outlet the normal gradients of k and ε are fixed equal to zero, which corresponds to the Neumann ('do-nothing') boundary condition. In the finite element framework, these homogeneous boundary conditions imply that the surface integrals resulting from integration in the variational formulation vanish [39].

$$\frac{\partial k}{\partial n} = 0 \quad (19)$$

$$\frac{\partial \varepsilon}{\partial n} = 0 \quad (20)$$

Moreover, a pressure value has to be assigned at the outlet section which is typically fixed at zero; however, to avoid numerical instabilities that hinder numerical convergence a hydrostatic pressure profile was assigned,

$$p = -g(z + D)(\rho_c(1 - \phi_0) + \rho_d \phi_0). \quad (21)$$

4.3.3. Near-wall treatment for turbulent flows

The Law of the Wall or Wall Function was used as depicted in Eq. (22) for the near wall treatment of the flow [40,41] in the numerical studies using a High Reynolds Turbulence Closure,

$$u_\tau = \frac{u}{\kappa \ln y^+ + B}. \quad (22)$$

The turbulence parameters κ and B values are 0.41 and 5.2, respectively [40].

5. Results and discussion

Prior to the solid-liquid suspensions experiments preliminary tests were performed with water under the experimental conditions depicted in Table 1, which allowed to verify if the MRI apparatus were suitably calibrated. The experimental 1D MRI velocity profiles were compared with numerical results from CFD simulations using the High Reynolds k - ε turbulence model [35]. These preliminary tests demonstrated a good agreement between the experimental and calculated results, thus, validating the correct calibration of the MRI apparatus.

5.1. 0.1–0.2 mm particles in 0.34 m ID pipe

The first tests were conducted with small spherical particles with size between 0.1–0.2 mm in the flow loop. As described in Table 1 the volumetric concentrations studied were 0.5, 1.0 and 3.0% (v/v) for flow rates of 1.0 and 2.0 l.s⁻¹. The numerical and experimental results, from both MRI and UVP, match quite well,

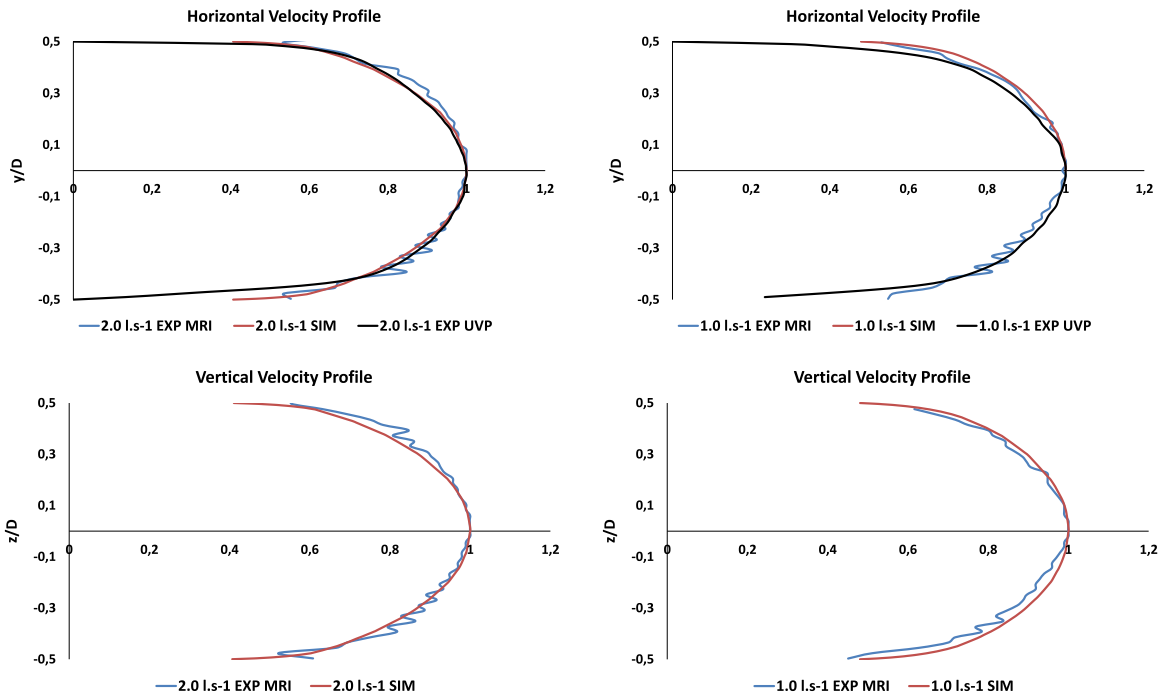


Fig. 6. Experimental MRI, UVP and Simulated normalized horizontal (Top) and vertical (Bottom) velocity profiles for flow rates of 2.0 (Left) and 1.0 l.s⁻¹ (Right) in a 34 mm ID pipe for a solids volumetric concentration of 0.5% (v/v) with 0.1–0.2 mm particles.

with negligible deviations, as presented in Figs. 6–8.

The UVP and MRI profiles, representing the velocities of the dispersed and continuous phases, respectively, are concordant with what was expected, since the Stokes Numbers for these particles is smaller than one, for all flow velocities tested (see Table 2), indicating that the particles follow the fluid streamlines for the three concentrations tested; in other words, the particle motion is tightly coupled with the motion of the fluid since there is very little slip between the phases. The simulated (mixture

model) and experimental values did, however, match quite well again, for this particle concentration.

5.2. 0.4–0.6 mm particles in 0.34 m ID pipe

Following the tests with the 0.1–0.2 mm particles, similar testing was performed with bigger particles with a size range of 0.4–0.6 mm, and a mean particle diameter of 0.5 mm. The same solids volumetric fractions and flow rates used for the 0.1–0.2 mm

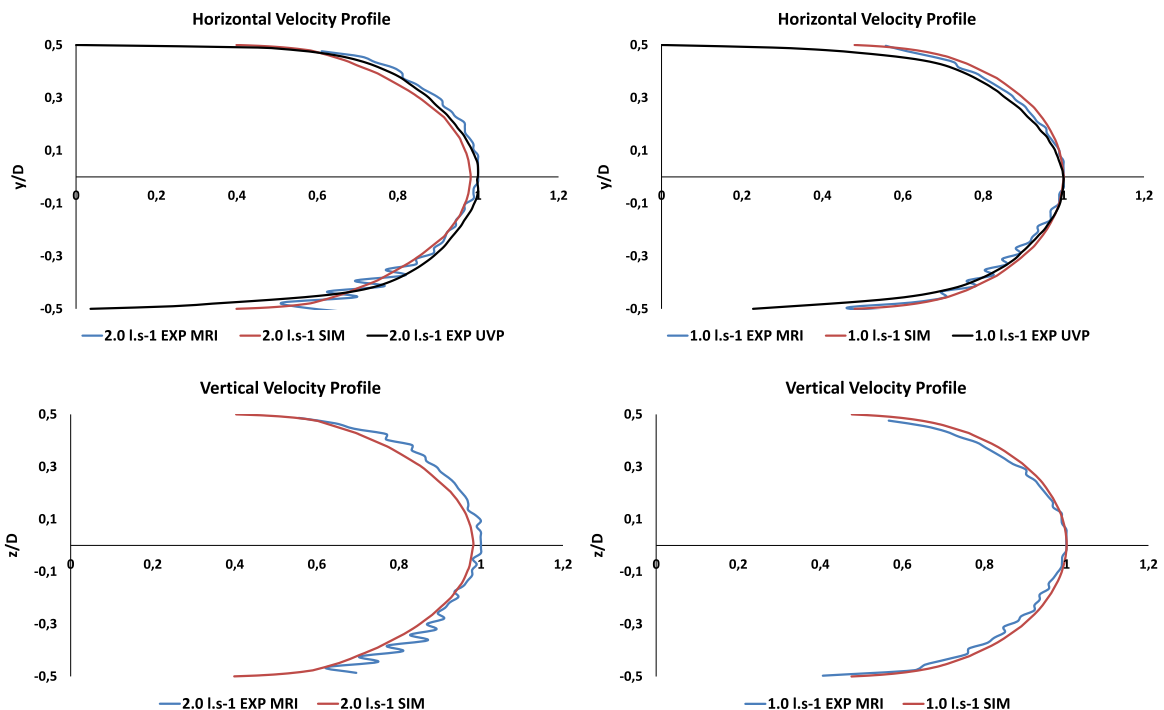


Fig. 7. Experimental MRI, UVP and Simulated normalized horizontal (Top) and vertical (Bottom) velocity profiles for flow rates of 2.0 (Left) and 1.0 l.s⁻¹ (Right) in a 34 mm ID pipe for a solids volumetric concentration of 1.0% (v/v) with 0.1–0.2 mm particles.

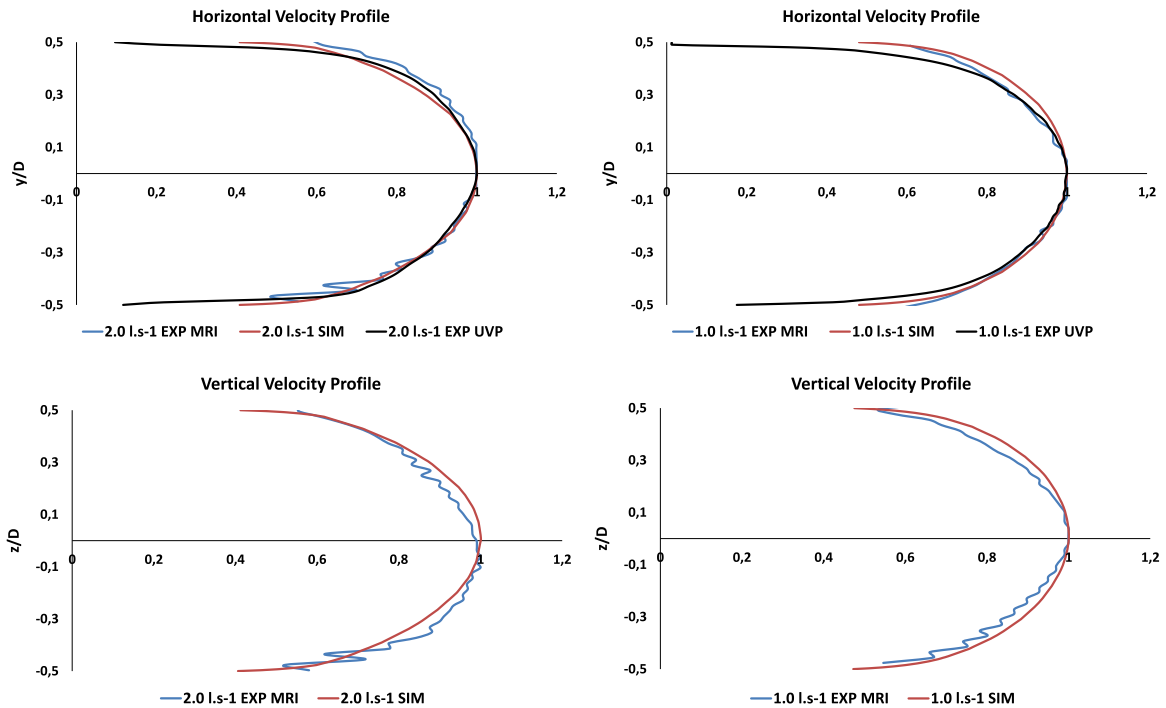


Fig. 8. Experimental MRI, UVP and Simulated normalized horizontal (Top) and vertical (Bottom) velocity profiles for flow rates of 2.0 (Left) and 1.0 l.s⁻¹ (Right) in a 34 mm ID pipe for a solids volumetric concentration of 3.0% (v/v) with 0.1–0.2 mm particles.

particles testing were employed for these trials. With these bigger particles, it can be seen from Fig. 9 to 11 that the numerical and MRI experimental velocity profiles present a good fit for all the concentrations tested. The UVP data, however, deserves some considerations as there are asymmetries, which should not occur for the horizontal profiles.

This lack of symmetry, rather than depicting a physical phenomenon, can result from the accumulation of particles in the posterior probe [42,43], thus, causing an obstruction in the signal

generation and acquisition for this probe (which is located in the right side of the flow direction as depicted in Fig. 3). Nevertheless, if the offset in the lower half of Figs. 10–12 is disregarded, and only the upper half of the UVP velocity profiles is considered, then it becomes apparent that the velocity profiles approach the MRI and mixture model numerical profiles, except when we come close to the wall. For the larger velocities, with a Stokes Number of 2.20, it was assumed that the mixture model application was still valid and the velocity profiles seem to further validate the assumption. Also,

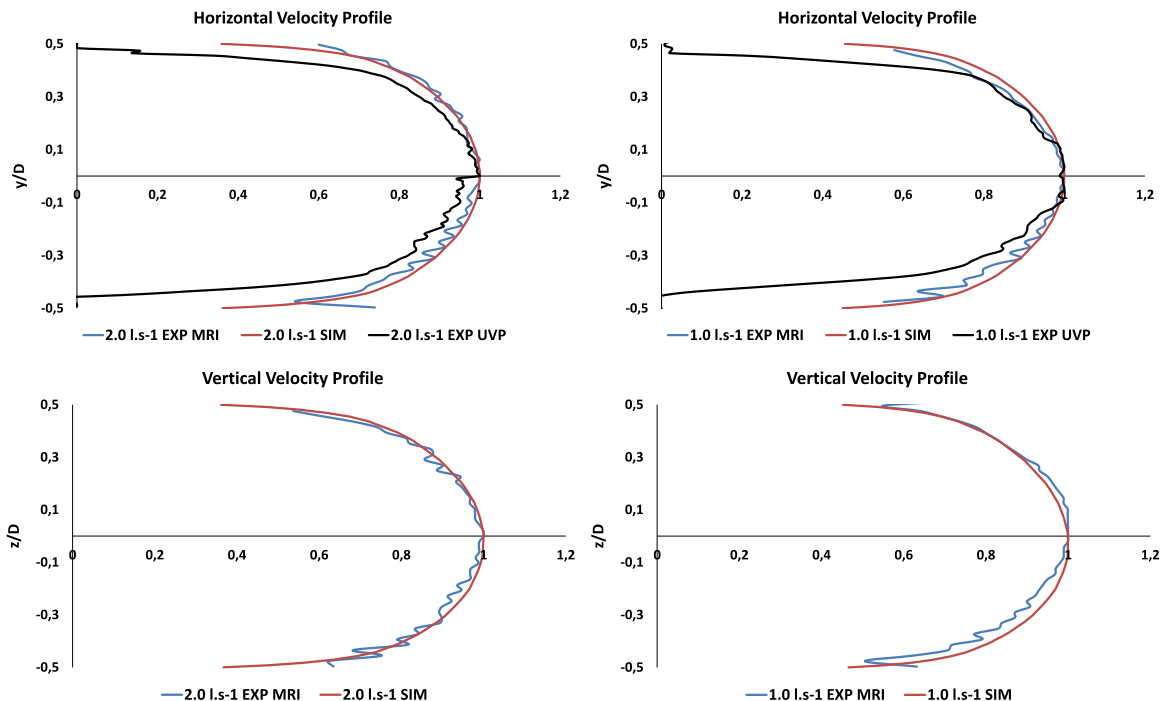


Fig. 9. Experimental MRI, UVP and Simulated normalized horizontal (Top) and vertical (Bottom) velocity profiles for flow rates of 2.0 (Left) and 1.0 l.s⁻¹ (Right) in a 34 mm ID pipe for a solids volumetric concentration of 0.5% (v/v) with 0.4–0.6 mm particles.

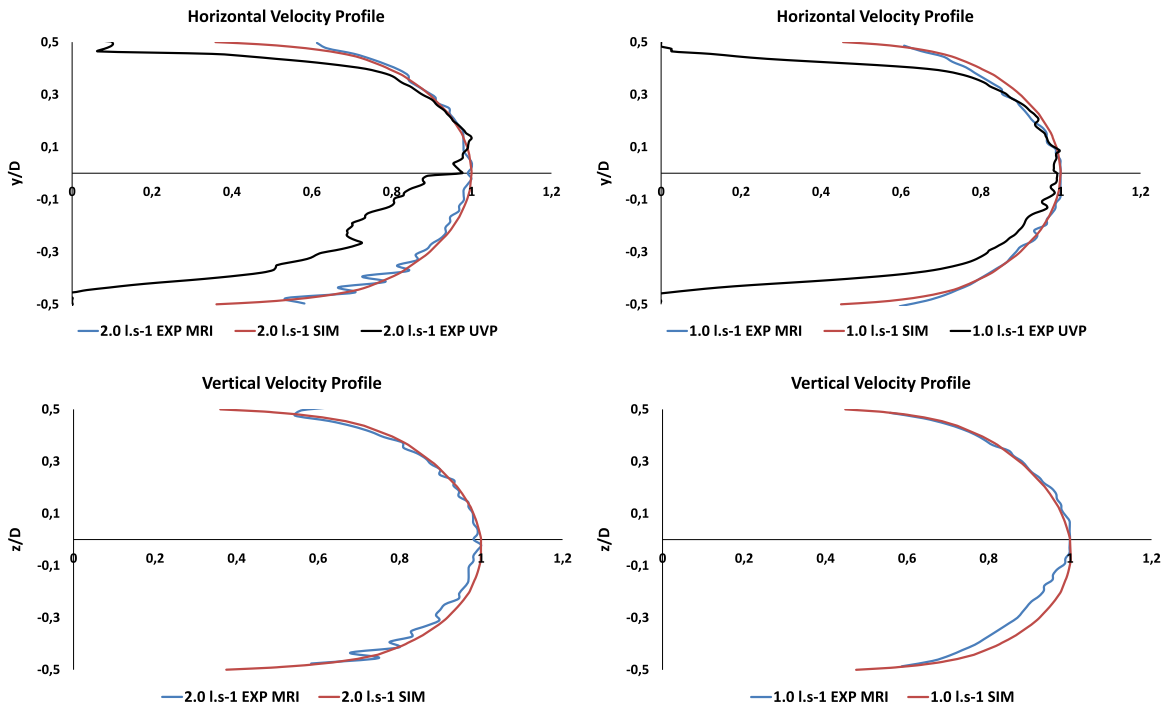


Fig. 10. Experimental MRI, UVP and Simulated normalized horizontal (Top) and vertical (Bottom) velocity profiles for flow rates of 2.0 (Left) and 1.0 l.s⁻¹ (Right) in a 34 mm ID pipe for a solids volumetric concentration of 1.0% (v/v) with 0.4–0.6 mm particles.

for the higher concentrations and lower flow velocity, it is apparent some asymmetry in the MRI vertical profiles and in the simulated ones, in agreement with the non-homogeneous distribution of these larger particles in the pipe cross-section, in opposition to what happened for the smaller particles.

5.3. 0.4–0.6 mm particles in 0.50 m ID pipe

In addition to the previous experiments it was also possible to

study solid-liquid suspensions using a pipe with a bigger internal diameter. The larger particles, with a size range of 0.4–0.6 mm, were tested in this pipe. The experimental conditions were as depicted in Table 1. With the 0.50 m ID pipe it was also possible to acquire vertical normalized distributions of conductivity, using the EIT system, that were used to infer on the distribution of particles in the pipe section (see Eqs. 1 to 5). For this technique to retrieve adequate images, the reference measurements were done without any particles in the flow rig. The reconstructed 2D images shown

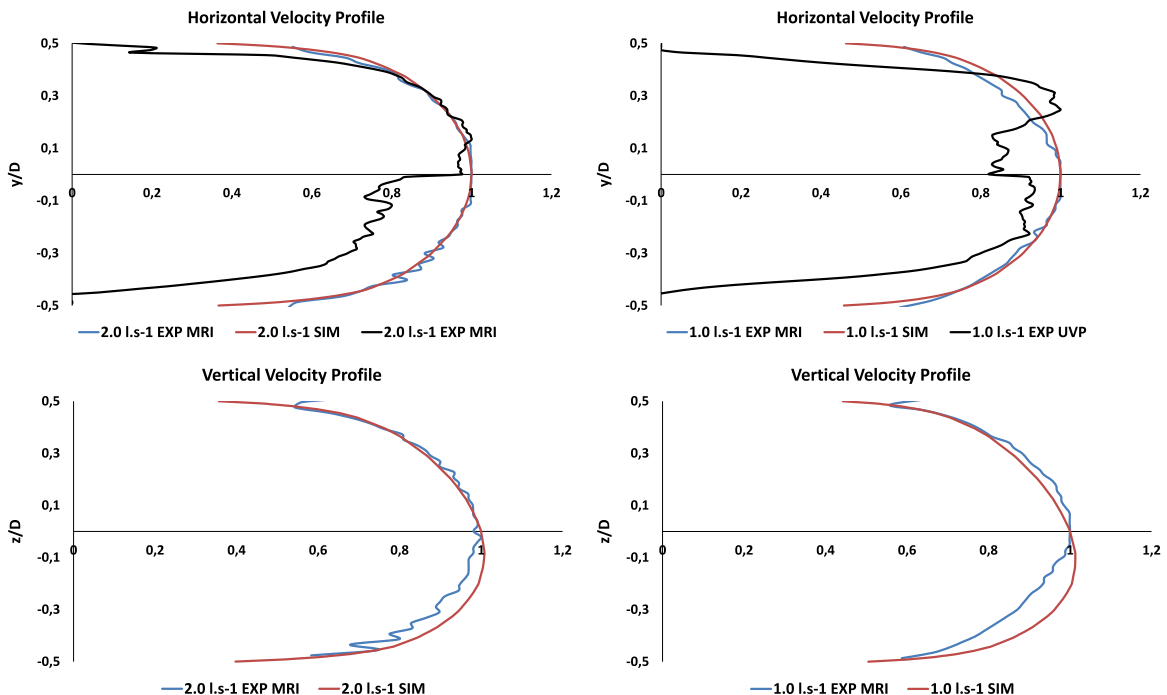


Fig. 11. Experimental MRI, UVP and Simulated normalized horizontal (Top) and vertical (Bottom) velocity profiles for flow rates of 2.0 (Left) and 1.0 l.s⁻¹ (Right) in a 34 mm ID pipe for a solids volumetric concentration of 3.0% (v/v) with 0.4–0.6 mm particles.

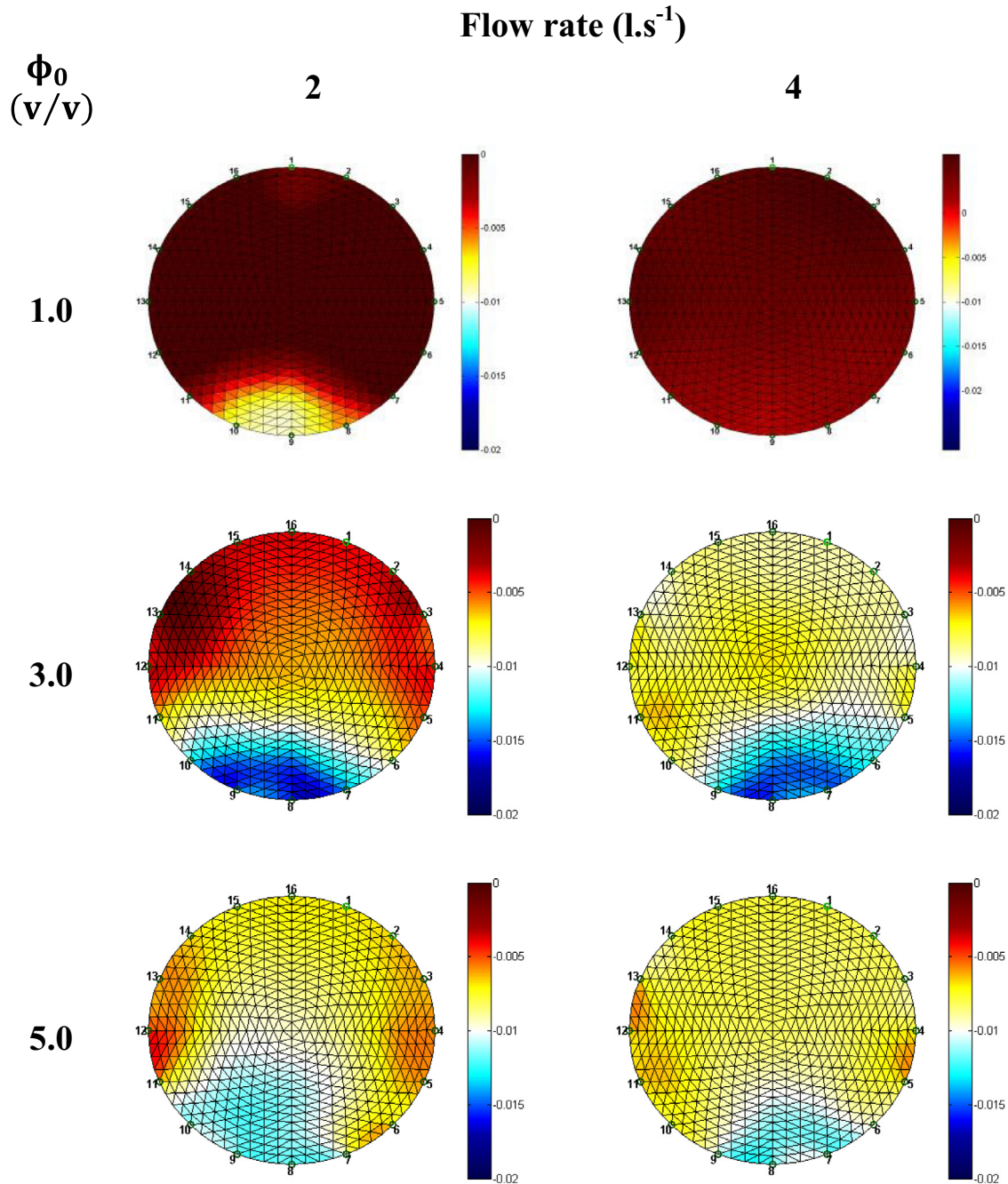


Fig. 12. Reconstructed 2D images of the pipe cross-section using EIT normalized conductivity measurements for solid–liquid suspensions of 0.4–0.6 mm particles for 1.0 (Top), 3.0 (Middle) and 5.0% (v/v) (Bottom) solids volumetric concentration in a 50 mm ID pipe.

in Fig. 12 represent normalized conductivity measurements, η . The normalization is performed using Eq. (1). From Fig. 12 it is possible to observe the effect of particle concentration on the conductivity gradient. For 1.0 and 3.0% (v/v) particle concentration at $2\text{ l}\cdot\text{s}^{-1}$ the colour change towards blue in the bottom of the images indicates an increase in particle concentration along the bottom of the pipe. The regions with a more intense red colour represent the areas where there is little change in the electrical conductivity, thus, meaning; little or no particles are present. Also, the effect of the flow velocity increase in the turbulent dispersion of particles is obvious by comparison of the left and right columns, demonstrated by the shift in the colour profiles towards the top of the colourbar, i.e., indicating a lower normalized electrical

conductivity difference between the mixture and the reference measurements.

At 5.0% (v/v) particle concentration it would be expected that the lower part of the image would be of a similar blue colour as in the 3.0% (v/v) reconstructed images, but corresponding to an even greater blue area, denoting a higher particle concentration at the bottom, due to the effect of gravity. This is, however, not the case when the two bottom reconstructed images in Fig. 12 are inspected in detail. The particles seem to be more fluidized as denoted by wider white and yellow areas. This colour arrangement, particularly at the lower flow velocities, appears to indicate the presence of strong particle–particle interactions, due to increased particle concentration, which is augmented with an increase in the

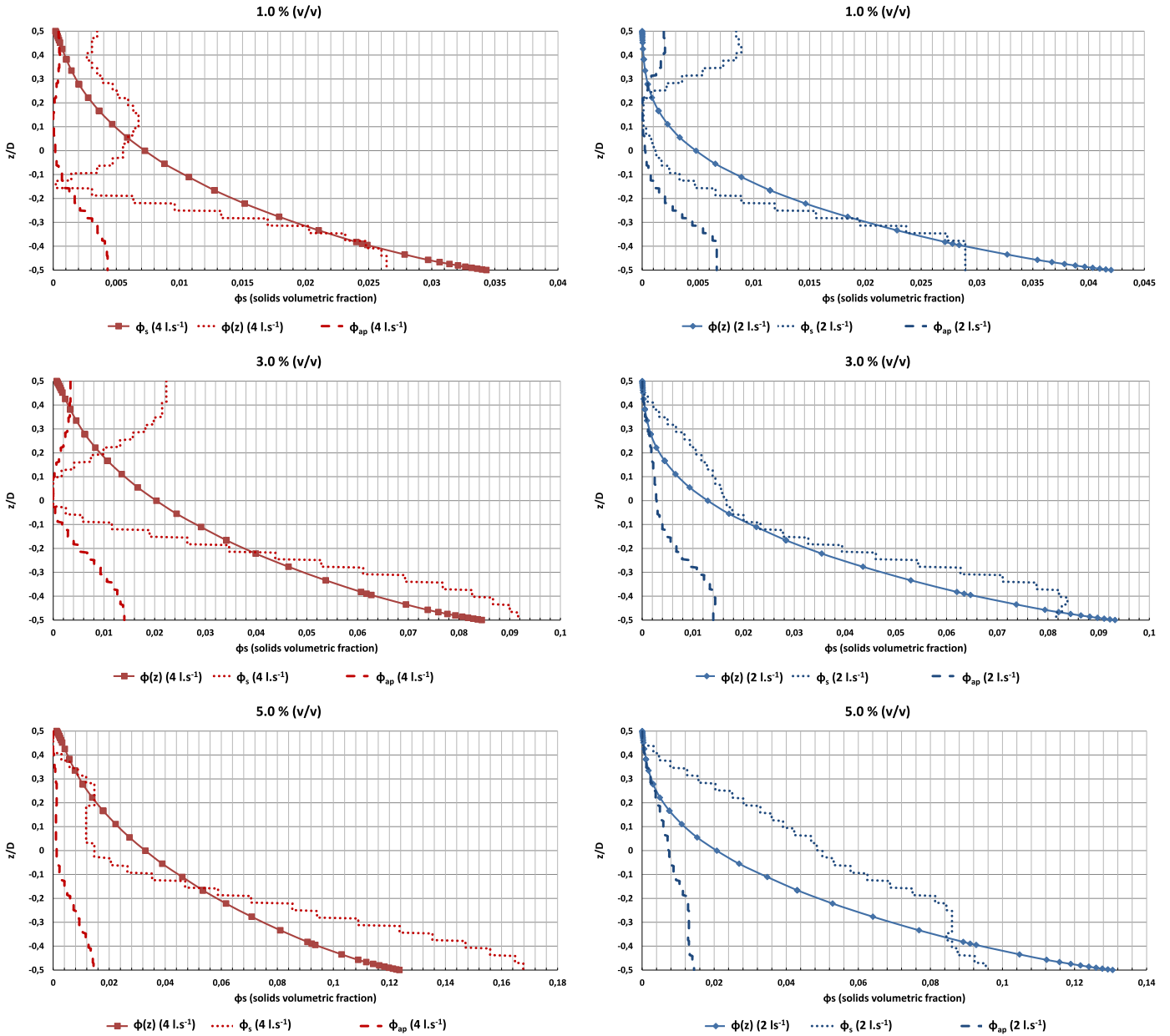


Fig. 13. Comparison between 1D calculated vertical particle distribution profiles with EIT, $\phi(z)$, and Maxwell Equation, ϕ_{ap} , with the particle concentrations profiles from the mixture model, ϕ_s , in a 50 mm ID pipe for the flowrates of 4.0 (Left Column) and 2.0 $l.s^{-1}$ (Right Column).

flow velocity.

The calculated vertical particle distribution profiles, based on the experimental and using both approaches depicted in Section III.C, as well as the numerical vertical particle distribution profiles from the mixture model, are presented in Fig. 13. The modified Maxwell Equation (see Eq. (3)), by comparison with the mixture model’s numerical values, underestimates the particle concentration values for most of the lower bottom half of the pipe section. This happens for all concentrations and flow velocities tested. With the second approach, Eq. (5), the particle concentration values are similar between the mixture model and the calculated values using EIT electrical conductivity data. Also, the trends predicted by the mixture model when flow rate increases (higher concentrations in the bottom of the pipe), are observed experimentally. For the 5.0% (v/v) concentration profile at 4 $l.s^{-1}$ deviation between numerical and experimental concentration in the bottom of the pipe, calculated using Eq. (5) is higher. This can be attributed to the ratio between the initial particle concentration

and the area under the curve in Eq. (5). As described above, a more fluidized mixture will result in a reduced normalized electrical conductivity profile, therefore, resulting in a smaller area under the curve. For area values below one, this ratio will result in an overshoot of the concentration profile as seen for the 5.0% (v/v) particle concentrations for a 4 $l.s^{-1}$ flow rate. Moreover, close to the top of the pipe, the uncertainty of the experimental measurements increases due to the lower signals in that region (lower number of particles, especially for the lower flow rates), and thus, agreement between numerical and experimental profiles is worse.

The MRI, UVP and numerical velocity profiles are presented in Figs. 14–16 and, overall, the normalized profiles seem to match for the UVP, MRI and numerical data sets. However, there are some discrepancies, in particular for the vertical velocity profile at the higher particle concentrations. For these experiments the UVP probes were vertically mounted for most of the experiments, and due to particle settling, the bottom probe acquisition was hindered considerably failing to provide any data. For the highest particle

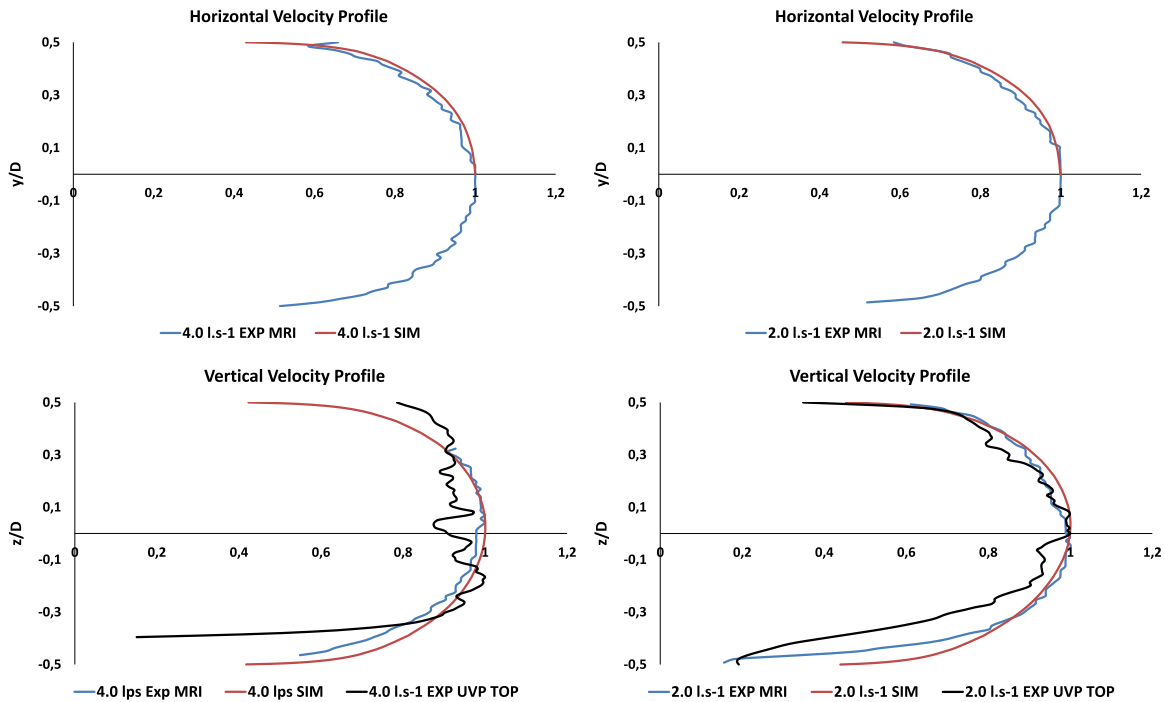


Fig. 14. Experimental MRI, UVP and Simulated normalized horizontal (Top) and vertical (Bottom) velocity profiles for solid–liquid suspensions of 0.4–0.6 mm particles with flow rates of 4.0 and 2.0 l.s⁻¹ in a 50 mm ID pipe for a solids volumetric concentration of 1.0% (v/v).

concentration (5.0% (v/v)) UVP data was obtained in both vertical and horizontal positions, as seen in Fig. 16.

The UVP profiles seem to become unreliable at the pipe centre area where the data is riddled with noise which can be attributed to the fact that only the probe on top of the pipe section was acquiring data. This is more notorious for the higher particle concentrations. In spite of the aforementioned noisy data, the vertical positioning of the probes did provide an opportunity to use UVP to recognize the effect of the flow velocity on the particle distribution gradients which seem to be concordant, in almost all the tests,

with both the MRI and the numerical data. The vertical asymmetry, which is more notorious for the higher concentration of particles, resulting from particle settling, is matched between the normalized experimental and the numerical profiles, although at the pipe bottom there are some deviations, especially for the lower velocity. Considering the visual inspection of the flows, the differences between the MRI and UVP profiles at the pipe bottom can be further explained by the presence of a moving bed where the particles slow the water velocity. The bigger offset at the pipe bottom observed in the UVP profiles can be explained by the lack

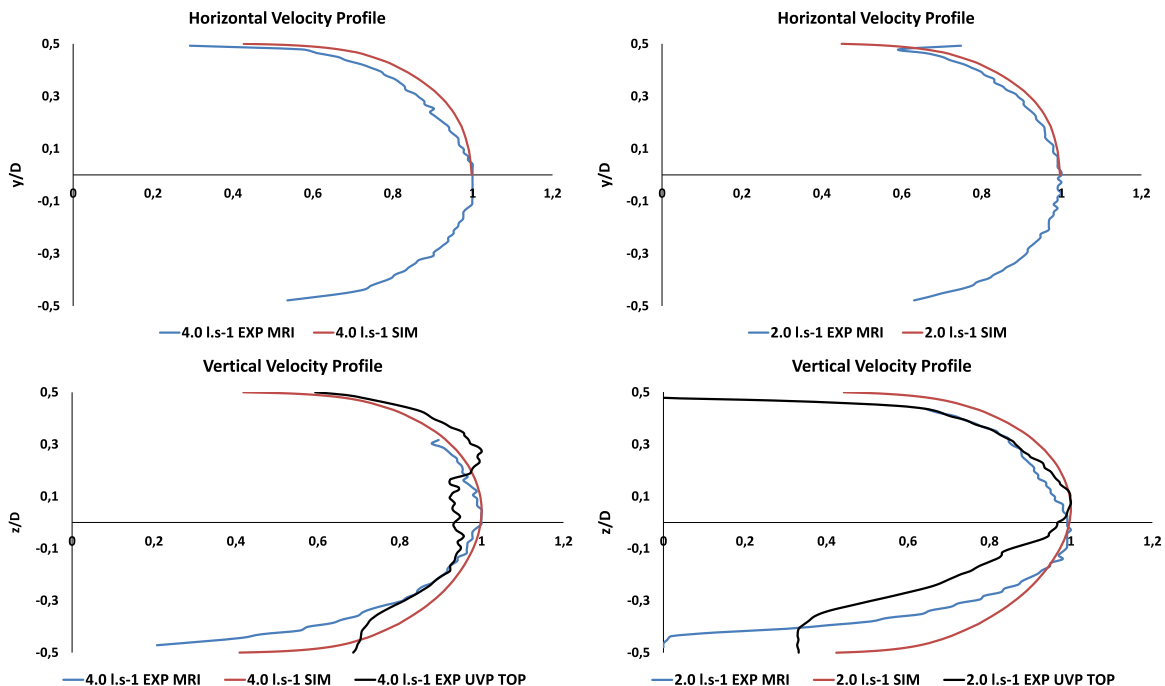


Fig. 15. Experimental MRI, UVP and Simulated normalized horizontal (Top) and vertical (Bottom) velocity profiles for solid–liquid suspensions of 0.4–0.6 mm particles with flow rates of 4.0 and 2.0 l.s⁻¹ in a 50 mm ID pipe for a solids volumetric concentration of 3.0% (v/v).

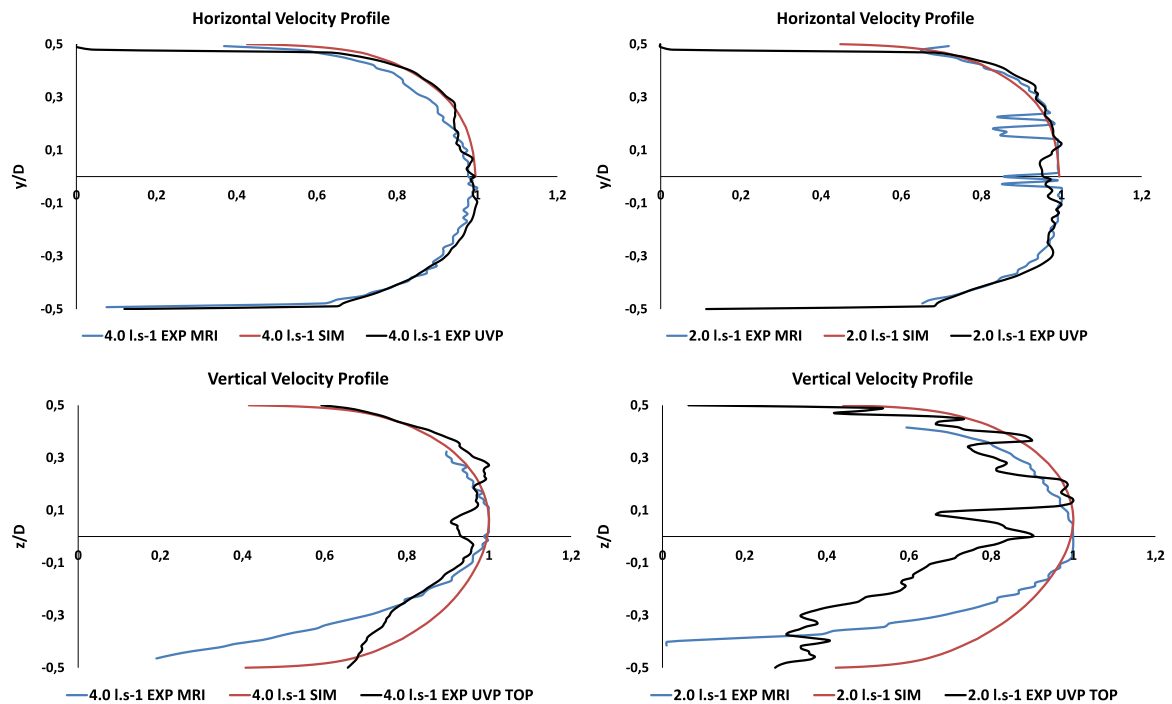


Fig. 16. Experimental MRI, UVP and Simulated normalized horizontal (Top) and vertical (Bottom) velocity profiles for solid-liquid suspensions of 0.4–0.6 mm particles with flow rates of 4.0 (Left) and 2.0 l.s⁻¹ (Right) in a 50 mm ID pipe for a solids volumetric concentration of 5.0% (v/v).

of data from the bottom probe and the increased impedance in the signal propagation due to increasing particle concentration.

Similarly to the previously presented studies, it was assumed that, for a Stokes Number of 1.66 (see Table 2), the mixture model application was still valid and again the velocity profiles seem to further validate the assumption, as seen in Figs. 14–16.

5.4. Pipe ID diameter effect for 0.4–0.6 mm particles

In the previous sections the influence of particle size and concentration were evaluated for different flow rates using the aforementioned experimental tomographic techniques. The influence of the flow loop's pipe diameter can only be evaluated by observing the behaviour of the 0.4–0.6 mm particles at 3.0% (v/v) at the highest flow rates since no experiments were carried out with the smaller particles for the 0.50 m ID pipe.

Comparing Figs. 11 and 15 it has already been stated that for the 0.50 m ID pipe there was a notorious asymmetry in the vertical velocity profile near the pipe bottom, as seen in Fig. 15, while in Fig. 11, for the smaller particles, there is little asymmetry, a more homogeneous distribution of particles in the pipe cross-section being displayed. These results can be attributed to stronger wall effects, i.e., particle shear induced phenomena in the 0.34 m ID pipe, explains a more accurate depiction by the mixture model in this case, since for the 0.34 m ID pipe tests there were more homogeneous distributions of particles.

6. Conclusions

The main objective of this study was to compare experimental data, from three different techniques, with numerical data from the mixture model for dilute solid-liquid suspensions flow, with the purpose of model validation. Experimental velocity profiles for both the liquid and solid phases employing Magnetic Resonance Imaging (MRI) and Ultrasonic Velocity Profiling (UVP), respectively, were attained, and particle distribution profiles in the pipe cross-

section were inferred from the Electrical Impedance Tomography (EIT) normalized conductivity distribution. From the results it is possible to conclude as follows:

1. For dilute flows, in both 0.34 and 0.50 m ID pipes, the attained 1D velocity profiles acquired with both the MRI and UVP techniques showed good agreement with each other and with the numerical results from the mixture model, although the UVP data exhibited some shortcomings: a small deviation in the angle between the probes can affect the data acquisition considerably, and the acquired information with the probe placed further downstream was, at times, affected by the presence of particle accumulation in the probe socket. This was visible by the increased noise in the UVP data with increasing particle concentration;
2. The effect of particle size and concentration on the flow was clear in the vertical MRI profiles in the 0.34 and 0.50 m ID pipe tests, where, for the bigger particles the effect of settling was more pronounced leading to asymmetrically profiles;
3. The EIT concentration profiles extended from the normalized electrical conductivity profiles showed good agreement with numerical data sets, particularly for higher concentrations of particles. In spite of some deviations, the method used in this work to calculate particle distributions from the normalized electrical distribution showed a better accuracy than the Maxwell Equation.

Acknowledgments

This work has been financially supported by the Fundação para a Ciência e Tecnologia, Project PTDC/EQU-EQU/66670/2006 and individual PhD scholarship SFRH/BD/79247/2011, by the COST Action FP1005 and by Strategic Research Centre Project Pest-C/EQB/UI0102/2013. The KAW foundation made it possible to acquire the MRI instrument.

References

- [1] S. Balachandar, J.K. Eaton, Turbulent dispersed multiphase flow, *Annu. Rev. Fluid Mech.* 42 (2010) 111–133, <http://dx.doi.org/10.1146/annurev.fluid.010908.165243>.
- [2] R. Silva, F.A.P. Garcia, P.M.G.M. Faia, M.G. Rasteiro, Settling suspensions flow modelling: A Review, *KONA Powder Part. J* 32 (2015) 1–16, <http://dx.doi.org/10.14356/kona.2015009>.
- [3] M. Nakagawa, S.A. Altobelli, A. Caprihan, E. Fukushima, E. Jeong, Experiments in Fluids Non-invasive measurements of granular flows by magnetic resonance imaging, *Exp. Fluids*. 60 (1993) 54–60.
- [4] a J. Sederman, L.F. Gladden, M.D. Mantle, Application of magnetic resonance imaging techniques to particulate systems, *Adv. Powder Technol.* 18 (2007) 23–38, <http://dx.doi.org/10.1163/15685520779768232>.
- [5] C.R. Müller, D.J. Holland, a J. Sederman, M.D. Mantle, L.F. Gladden, J. F. Davidson, Magnetic Resonance Imaging of fluidized beds, *Powder Technol.* 183 (2008) 53–62, <http://dx.doi.org/10.1016/j.powtec.2007.11.029>.
- [6] T. Dyakowski, L.F.C. Jeanmeure, A.J. Jaworski, Applications of electrical tomography for gas–solids and liquid–solids flows - A review, *Powder Technol.* 112 (2000) 174–192, [http://dx.doi.org/10.1016/S0032-5910\(00\)00292-8](http://dx.doi.org/10.1016/S0032-5910(00)00292-8).
- [7] C.G. Xie, N. Reinecke, M.S. Beck, D. Mewes, R.A. Williams, Electrical tomography techniques for process engineering applications, *Chem. Eng. J. Biochem. Eng. J.* 56 (1995) 127–133, [http://dx.doi.org/10.1016/0923-0467\(94\)02907-5](http://dx.doi.org/10.1016/0923-0467(94)02907-5).
- [8] Y. Takeda, Velocity profile measurement by ultrasonic doppler method, *Exp. Therm. Fluid Sci.* 1777 (1995) 444–453.
- [9] Y. Takeda, Ultrasonic Doppler method for velocity profile measurement in fluid dynamics and fluid engineering, *Exp. Fluids*. 26 (1999) 177–178, <http://dx.doi.org/10.1007/s003480050277>.
- [10] J. a Wiklund, M. Stading, a. J. Pettersson, A. Rasmuson, A comparative study of UVP and LDA techniques for pulp suspensions in pipe flow, *AIChE J.* 52 (2006) 484–495, <http://dx.doi.org/10.1002/aic.10653>.
- [11] Y. Ozaki, T. Kawaguchi, Y. Takeda, K. Hishida, M. Maeda, High time resolution ultrasonic velocity profiler, *Exp. Therm. Fluid Sci.* 26 (2002) 253–258, [http://dx.doi.org/10.1016/S0894-1777\(02\)00134-6](http://dx.doi.org/10.1016/S0894-1777(02)00134-6).
- [12] R.L. Powell, Experimental techniques for multiphase flows, *Phys. Fluids* 20 (2008) 040605, <http://dx.doi.org/10.1063/1.2911023>.
- [13] C.T. Crowe, *Multiphase Flow Handbook*, CRC Press - Taylor & Francis Group, Boca Raton, 2005.
- [14] J. Chaouki, F. Larachi, M.P. Dudukovic, Noninvasive tomographic and velocimetric monitoring of multiphase flows, *Ind. Eng. Chem. Res.* 5885 (1997) 4476–4503, <http://dx.doi.org/10.1021/ie970210t>.
- [15] L.F. Gladden, Nuclear magnetic resonance in chemical engineering: Principles and applications, *Chem. Eng. Sci.* 49 (1994) 3339–3408, [http://dx.doi.org/10.1016/0009-2509\(94\)00129-4](http://dx.doi.org/10.1016/0009-2509(94)00129-4).
- [16] T.-Q. Li, R.L. Powell, M.J. McCarthy, K. McCarthy, Velocity measurements of fiber suspensions in pipe flow by the nuclear magnetic resonance imaging method, *TAPPI J.* 77 (1994) 145–149.
- [17] R. Kotzé, J. Wiklund, R. Haldenwang, Optimisation of Pulsed Ultrasonic Velocimetry system and transducer technology for industrial applications, *Ultrasonics* 53 (2013) 459–469, <http://dx.doi.org/10.1016/j.ultras.2012.08.014>.
- [18] P. Krochak, R. Holm, M. Hirota, F. Lundell, D. Söderberg, A comparative study of semi-dilute fibre suspension flow using magnetic resonance imaging and ultrasonic Doppler velocimetry: Differences between fluid and fibre motion, in: *Int. Conf. Multi-Phase Flow*, Jeju, South Korea, 2013.
- [19] P.M. Faia, R. Silva, M.G. Rasteiro, F. a P. Garcia, a R. Ferreira, M.J. Santos, et al., Imaging particulate two-phase flow in liquid suspensions with electric impedance tomography, *Part. Sci. Technol.* 30 (2012) 329–342, <http://dx.doi.org/10.1080/02726351.2011.575444>.
- [20] M.G. Rasteiro, R. Silva, F.A.P. Garcia, P.M. Faia, Electrical tomography: a review of configurations and applications to particulate processes, *KONA Powder Part. J.* (2011) 67–80, <http://dx.doi.org/10.14356/kona.2011010>.
- [21] N. Polydorides, W.R.B. Lionheart, A matlab toolkit for three-dimensional electrical impedance tomography: a contribution to the electrical impedance and diffuse optical reconstruction software project, *Meas. Sci. Technol.* 13 (2002) 1871–1883, <http://dx.doi.org/10.1088/0957-0233/13/12/310>.
- [22] M. Vauhkonen, D. Vadasz, P.A. Karjalainen, E. Somersalo, J.P. Kaipio, Tikhonov regularization and prior information in electrical impedance tomography, *IEEE Trans. Med. Imaging.* 17 (1998) 285–293, <http://dx.doi.org/10.1109/42.700740>.
- [23] K.S. Cheng, D. Isaacson, J.C. Newell, D.G. Gisser, Electrode models for electric current computed tomography, *IEEE Trans. Biomed. Eng.* 36 (1989) 918–924, <http://dx.doi.org/10.1109/10.35300>.
- [24] Y. Fangary, R. Williams, W. Neil, J. Bond, I. Faulks, Application of electrical resistance tomography to detect deposition in hydraulic conveying systems, *Powder Technol.* (1998).
- [25] M. Wang, T. Jones, R. Williams, Visualization of asymmetric solids distribution in horizontal swirling flows using electrical resistance tomography, *Chem. Eng. Res. Des.* 81 (2003) 854–861, <http://dx.doi.org/10.1205/02637603322482095>.
- [26] R. Giguère, L. Fradette, D. Mignon, P. a Tanguy, Characterization of slurry flow regime transitions by ERT, *Chem. Eng. Res. Des.* 86 (2008) 989–996, <http://dx.doi.org/10.1016/j.cherd.2008.03.014>.
- [27] M. Manninen, V. Taivassalo, S. Kallio, *On the mixture model for multiphase flow*, VTT Publications, Espoo, 1996.
- [28] M. Ishii, T. Hibiki, *Thermo-Fluid Dynamics of Two-Phase Flow*, 2nd Ed, Springer, New York, 2011.
- [29] D.R. Kaushal, Y. Tomita, Prediction of concentration distribution in pipeline flow of highly concentrated slurry, *Part. Sci. Technol.* 31 (2013) 28–34, <http://dx.doi.org/10.1080/02726351.2011.639045>.
- [30] G.V. Messa, M. Malin, S. Malavasi, Numerical prediction of fully-suspended slurry flow in horizontal pipes, *Powder Technol.* 256 (2014) 61–70, <http://dx.doi.org/10.1016/j.powtec.2014.02.005>.
- [31] F. Yilmaz, M.Y. Gundogdu, Analysis of conventional drag and lift models for multiphase CFD modeling of blood flow, *Korea-Aust. Rheol. J* 21 (2009) 161–173.
- [32] K. Hiltunen, A. Jäsberg, S. Kallio, H. Karema, M. Kataja, A. Koponen, et al., *Multiphase flow dynamics: Theory and numerics*, VTT Publications, Espoo, 2009.
- [33] R. Silva, C. Cotas, F.A.P. Garcia, P.M. Faia, M.G. Rasteiro, Particle distribution studies in highly concentrated solid–liquid flows in pipe using the mixture model, *Procedia Eng.* 102 (2015) 1016–1025, <http://dx.doi.org/10.1016/j.proeng.2015.01.224>.
- [34] M.J. Pang, J.J. Wei, Analysis of drag and lift coefficient expressions of bubbly flow system for low to medium Reynolds number, *Nucl. Eng. Des.* 241 (2011) 2204–2213, <http://dx.doi.org/10.1016/j.nucengdes.2011.03.046>.
- [35] D.C. Wilcox, *Turbulence Modeling for CFD*, 3rd Ed, DCW Industries, Inc., 2006.
- [36] K. Ekambara, R.S. Sanders, K. Nandakumar, J.H. Masliyah, Hydrodynamic simulation of horizontal slurry pipeline flow using ANSYS-CFX, *Ind. Eng. Chem. Res.* 48 (2009) 8159–8171, <http://dx.doi.org/10.1021/ie801505z>.
- [37] E.A. Toorman, Validation of macroscopic modelling of particle-laden turbulent flows, in: *6th Belgian Natl. Congr. Theor. Appl. Mech.*, Gent, 2003.
- [38] H. Versteeg, W. Malalasekera, *An introduction to computational fluid dynamics: the finite volume method*, 2nd ed, Prentice Hall, 2007.
- [39] D. Kuzmin, O. Mierka, S. Turek, On the implementation of the κ - ϵ turbulence model in incompressible flow solvers based on a finite element discretisation, *Int. J. Comput. Sci. Math.* 1 (2007) 193, <http://dx.doi.org/10.1504/IJCSM.2007.016531>.
- [40] COMSOL Multiphysics, *COMSOL Multiphysics User Guide Version 4.3.a*, (2012).
- [41] T. Cebeci, *Analysis of Turbulent Flows with Computer Programs*, Elsevier, 2004.
- [42] J. Wiklund, M. Stading, Application of in-line ultrasound Doppler-based UVP-PD rheometry method to concentrated model and industrial suspensions, *Flow. Meas. Instrum.* 19 (2008) 171–179, <http://dx.doi.org/10.1016/j.flowmeasinst.2007.11.002>.
- [43] T. Wang, J. Wang, F. Ren, Y. Jin, Application of Doppler ultrasound velocimetry in multiphase flow, *Chem. Eng. J.* 92 (2003) 111–122, [http://dx.doi.org/10.1016/S1385-8947\(02\)00128-6](http://dx.doi.org/10.1016/S1385-8947(02)00128-6).